surfaces

MDPI

Communication

Strain Induced Phase Transition of WS_2 by Local Dewetting of Au/Mica Film upon Annealing

Tomasz Kosmala [1], Pawel Palczynski [2], Matteo Amati [3], Luca Gregoratti [3], Hikmet Sezen [3], Cecilia Mattevi [2], Stefano Agnoli [1,*] and Gaetano Granozzi [1]

[1] Dipartimento di Scienze Chimiche, Università di Padova, Via Marzolo 1, 35131 Padova, Italy; tomasz.kosmala@unipd.it (T.K.); gaetano.granozzi@unipd.it (G.G.)
[2] Department of Materials, Imperial College, London SW7 2AZ, UK; P.Palczynski@imperial.ac.uk (P.P.); c.mattevi@imperial.ac.uk (C.M.)
[3] Elettra-Sincrotrone Trieste S.C.p.A., SS14, km 163.5 in AREA Science Park, 34149 Trieste-Basovizza, Italy; matteo.amati@elettra.eu (M.A.); luca.gregoratti@elettra.eu (L.G.); Hikmet.Sezen@elettra.eu (H.S.)
* Correspondence: stefano.agnoli@unipd.it

Abstract: Here, we present a proof-of-concept experiment where phase engineering at the nanoscale of 2D transition metal dichalcogenides (TMDC) flakes (from semiconducting 2H phase to metallic 1T phase) can be achieved by thermal annealing of a TMDC/Au/mica system. The local dewetting of Au particles and resulting tensile strain produced on the TMDC flakes, strongly bound to the Au surface through effective S-Au bonds, can induce a local structural phase transition. An important role is also played by the defects induced by the thermal annealing: when vacancies are present, the threshold strain needed to trigger the phase transition is significantly reduced. Scanning photoelectron microscopy (SPEM) was revealed to be the perfect tool to monitor the described phenomena.

Keywords: transition metal dichalcogenides; strain engineering; phase transition; photoelectron microscopy

Citation: Kosmala, T.; Palczynski, P.; Amati, M.; Gregoratti, L.; Sezen, H.; Mattevi, C.; Agnoli, S.; Granozzi, G. Strain Induced Phase Transition of WS_2 by Local Dewetting of Au/Mica Film upon Annealing. *Surfaces* **2021**, *4*, 1–8. https://dx.doi.org/10.3390/surfaces4010001

Received: 30 November 2020
Accepted: 18 December 2020
Published: 22 December 2020

1. Introduction

In recent years, 2D transition metal dichalcogenides (TMDCs) [1] have gathered a great deal of interest because of their potential applications in catalysis [2,3], optoelectronic and electronic devices [4,5], and energy conversion systems [6]. TMDCs have a general MX_2 formula, where M is a transition metal (e.g., V, Mo, W), and X a chalcogen (i.e., S, Se, Te). Differently from graphene, single layer TMDCs have a sandwich structure, where the upper and lower layers consist of chalcogen atoms, and a plane of transition metal ions is sandwiched in between. Depending on the specific stacking of the different layers (see Figure 1), many polymorphs (labelled as 2H and 1T), which exhibit rather different properties, can be found: the 2H phase with a trigonal prismatic coordination of the metal is a semiconductor, while the 1T phase, with octahedral coordination of the metal cations, has a metallic nature. Therefore, the 2H to 1T transition impacts most functional properties: the 2H phase is a poor electrocatalyst, but an excellent light absorber with strong photoluminescence, whereas the 1T phase is catalytically very active, and a good electron conductor, however being metallic, it does not show optical absorption/emission properties [7,8]. Moreover, the ability of creating conductive and semiconductive heterojunctions within the same material can be clearly exploited for the realization of molecular scale electronic devices with atomically thin 2D layers [9]. Given those radically different properties of 2H and 1T, the control at the nanoscale of the crystalline phase of the TMDCs is important to achieve the desired properties in the final devices.

Within this context, the strain engineering method [10] represents a suitable route to tailor materials properties by modifying mechanical or structural features. In this respect, 2D TMDCs are particularly suitable for strain engineering because they can tolerate large

strain [11,12]. Indeed, there are examples where phase transitions from the semiconducting 2H phase to the metallic 1T one can be triggered by mechanical strain [11,13,14]

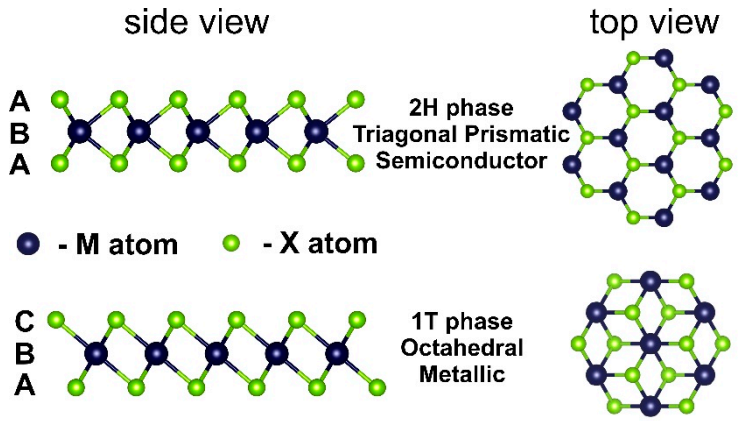

Figure 1. Different structural models of the 2H and 1T polymorphs in a MX_2 monolayer.

Herein, we present experimental results that demonstrate that WS_2 flakes can be phase engineered at the nanoscale when transferred on Au/mica thin films: thanks to a thermally activated dewetting of the gold layer, producing a highly corrugated surface, a strain induced phase transition can be triggered. As a matter of fact, it is well known from the literature that as a consequence of annealing, sub-micrometer-size bubbles are formed by gases trapped at the interface between Au film and mica substrate [15–18] leading to a local dewetting of the Au film. For the first time, we demonstrate here that the such microbubbles can induce a tensile strain on WS_2 flakes, inducing a local structural phase transition from the semiconducting 2H to the metallic 1T phase. This is the direct consequence of the strong WS_2/Au interaction that is enabled by the high chemical affinity between sulfur and Au [19].

2. Materials and Methods

Mono-/bilayer WS_2 flakes were grown by chemical vapor deposition (CVD) on a SiO_2/Si substrate starting from commercial powders of WO_3 and sulfur at a temperature of 800 °C. Then they were transferred onto commercial Au/mica thin films (150 nm) by the wet-transfer technique [20]. More details can be found in the original paper. The final WS_2/Au/mica heterostructures were then annealed in ultra-high-vacuum (UHV) according to the following procedure: the temperature was raised from room temperature (RT) to 750 K with a rate of 4 K min^{-1}, then the sample was constantly annealed at 750 K for 5 h and finally the temperature was raised to 830 K with a rate of 4 K min^{-1}, and after 40 min the samples was cooled down to RT. Such annealing was monitored by scanning photoelectron microscopy (SPEM) at the ESCAmicroscopy beamline of Elettra synchrotron radiation facility (Trieste, Italy) [21]. The SPEM imaging mode can map elemental species and their chemical state by collecting the photoelectrons emitted in a selected kinetic energy (KE) window, with a 48 channels detector, while raster-scanning the sample with a microbeam focused down to a 120 nm spot [22]. The results are photoemission intensity maps acquired with lateral resolution in the 100 nm range [22] where each point is a spectrum in the selected energy windows. For the best spectral resolution (down to 0.2 eV), microspot photoemission (μ-PE) spectra from the same focused spot was acquired. A photon energy of 652.15 eV was used for all the SPEM measurements. Scanning electron microscopy (SEM) images were obtained using a Zeiss Supra 35VP equipment. Raman spectra were acquired with a ThermoFisher DXR Raman microscope using a 532 nm laser (0.1 mW), focused on the sample with a 50× objective (Olympus) obtaining a spot size of about 1.1 μm.

3. Results and Discussion

The W 4f and S 2p SPEM maps recorded at room temperature (RT) are shown in Figure 2a,b, respectively. These images clearly show the well-defined presence of the WS_2 flake on the Au/mica substrate, and confirm the successful transfer of the WS_2 flakes. Moreover, in both the W 4f and S 2p maps, we can distinguish two regions of different intensity, labelled as ML (monolayer) and BL (bilayer) in Figure 2a,b. Interestingly, in the photoemission spectra extracted from the W4f and S2p maps in the ML or BL regions (see insets in Figure 2a,b, respectively) no binding energy (BE) shift is observed, only a different intensity. Raman Spectroscopy data confirm the presence of single or bilayer highly crystalline 2H-WS_2 [20]. Moreover, within the flakes some holes of 0.5–2.0 μm can be observed (blue color), which most probably are induced by the transfer process. The single energy distribution curve of photoemission spectra in the W 4f and S 2p region for the monolayer WS_2 are reported in Figure 2c,d, respectively. The peaks at a BE of 32.7 and 34.9 eV correspond to the W 4f photoemission doublet, while the features at 162.4 eV and 163.6 eV can be ascribed to S $2p_{3/2}$ and S $2p_{1/2}$ levels, respectively. These BE positions are typical of W^{4+} and S^{2-} in 2H-WS_2 [23–25]. No other components have been detected, which indicates phase purity of the flake on the specific point. Furthermore, a S:W ratio equal to 2.0:1.0, as expected for a stoichiometric defect free layer, was deduced by the μ-PE intensities (see Table 1). The SPEM maps were obtained on several different flakes distributed on the Au/mica substrate and the results were highly reproducible.

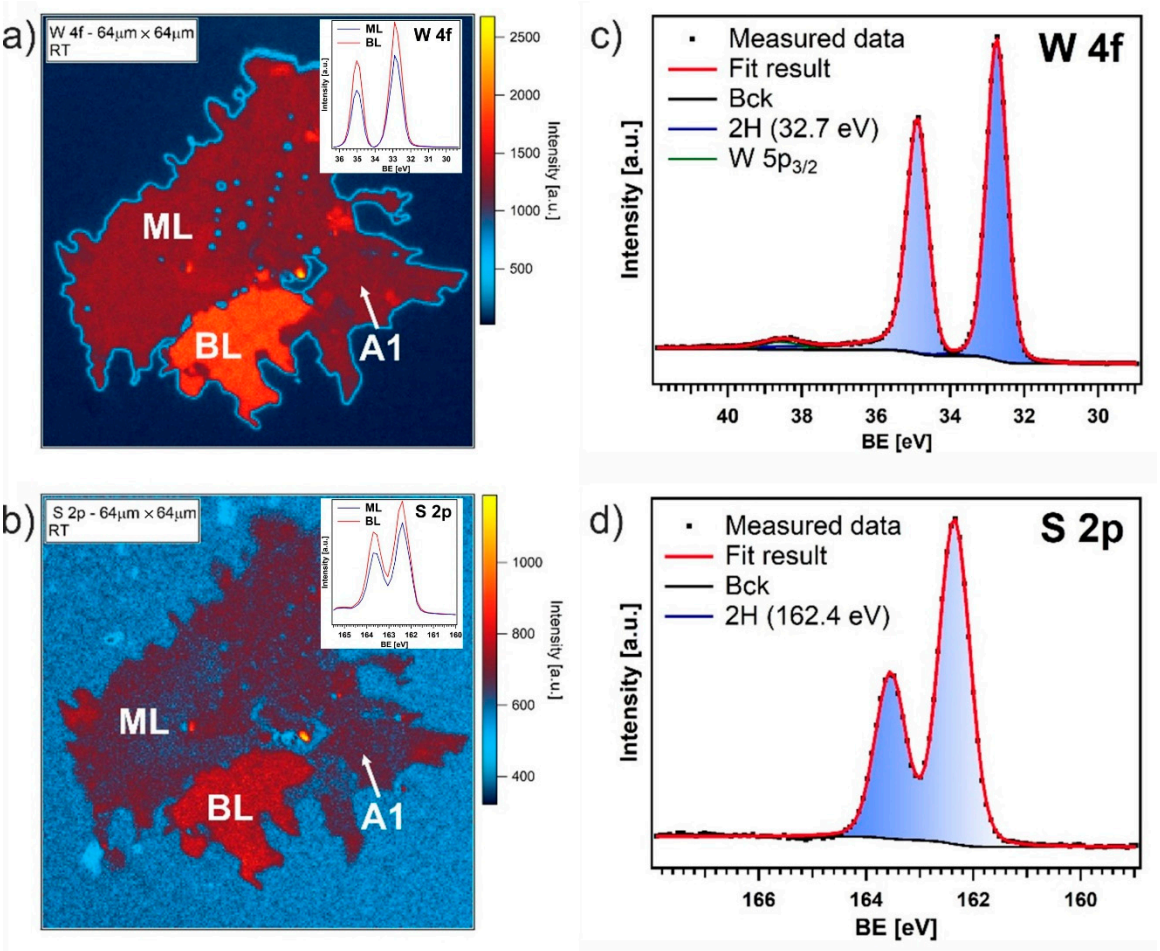

Figure 2. W 4f (**a**) and S 2p (**b**) SPEM maps recorded at room temperature (RT) in the binding energy (BE) range of 29.3–37.0 eV and 158.5–166.2 eV, respectively. W 4f (**c**) and S 2p (**d**) single energy distribution curve of microspot photoemission (μ-PE) spectra acquired at A1 point.

Table 1. Relevant quantitative μ-PE data in different spots of the flakes (see Figures 2 and 3). The data have been derived from the chemically shifted components of W and S after deconvolution of the core level spectra.

	W 4f [at.%]	S 2p [at.%]	S 2p/W 4f	W 4f 2H [%]	W 4f 1T [%]	W 4f Metal [%]	S 2p 2H [%]	S 2p 1T [%]	2H S 2p/W 4f	1T S 2p/W 4f
A1 RT	32.9	67.1	2.04	100	0	0	100	0	2.04	-
A2 750 K (basal site)	33.4	66.6	1.99	100	0	0	100	0	1.99	-
B1 750 K	34.9	65.1	1.86	90.8	1.9	7.5	98.0	2.0	2.01	1.96
B2 750 K	37.2	62.6	1.68	78.2	4.6	17.2	94.7	5.3	2.03	1.94
B3 830 K	47.3	52.7	1.11	53.5	13.5	33.0	81.1	18.9	1.69	1.56

The changes of the chemical composition of 2H-WS_2 flakes as a consequence of thermal treatment in UHV have been monitored in real-time in front of the SPEM, using the W 4f core level spectra (29.75–37.45 eV) in the same spatial region of Figure 2a. A series of maps obtained after different thermal treatments is reported in Figure 3a–c.

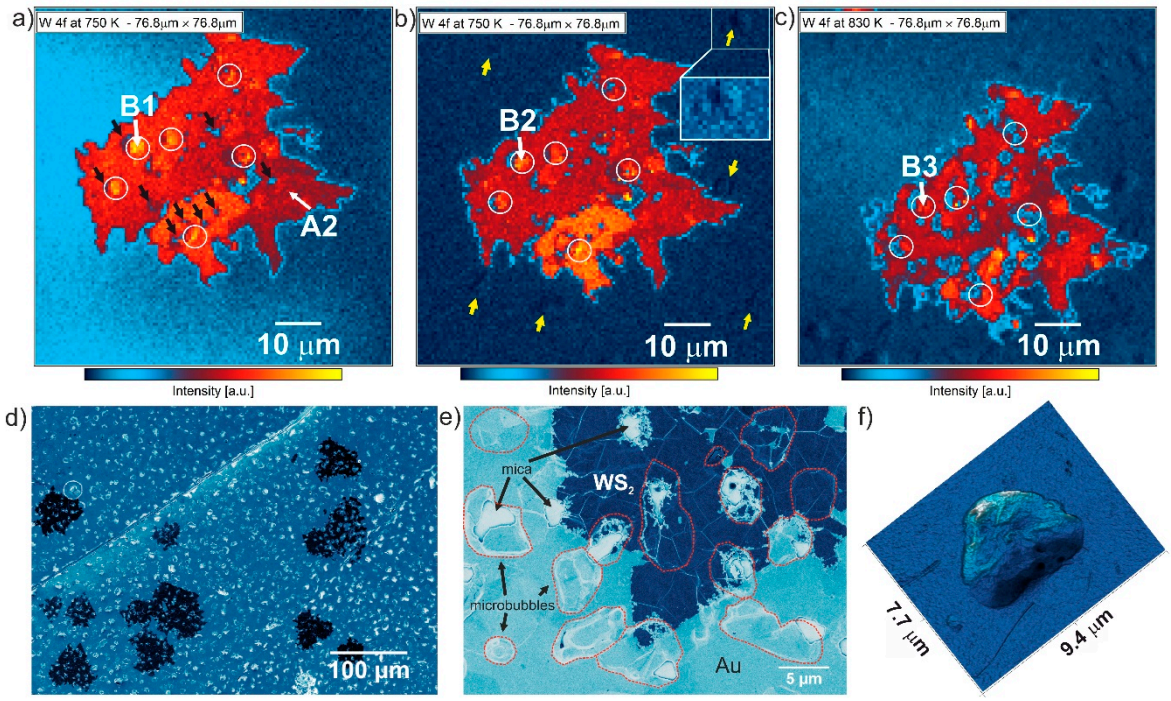

Figure 3. W 4f SPEM maps after different in situ annealing treatments: (**a**) Recorded immediately after reaching 750 K; (**b**) 750 K recorded 1 h later than (**a**); (**c**) recorded immediately after reaching 830 K. The capital letters B1, B2 and B3 indicate the points where single energy distribution curve was obtained for W 4f and S 2p. In (**b**) an insert is reported to outline the formation of lenticular gold particles (see text). (**d**,**e**) SEM images obtained ex situ after a thermal treatment at 830 K. (**f**) 3D SEM micrograph outlining the microbubbles generated after the annealing.

The SPEM W 4f map when the 750 K temperature is reached is shown in Figure 3a. First of all, new bright features appear on the basal plane of WS_2, which are marked by white circles. Additionally, new holes (marked by black arrows) became apparent within the flake, indicating that at this temperature a partial degradation of the material takes place. Figure 3b, recorded after 1h of constant annealing, does not show any further significant change in the distribution of the photoemission intensity of the W 4f signal;

however, new features, indicated by yellow arrows, can be observed on the gold support around the flake (see inset in Figure 3b). Notably, these features present a peculiar intensity modulation with a brighter side and a darker one. This contrast was energy independent, therefore it is not related to a difference in the chemical composition, but to a morphological effect (i.e., a change in the intensity of the emitted photoelectrons due to the local surface orientation), and it can be explained by the formation of 3D gold structures.

The further increase of the temperature to 830 K in UHV (Figure 3c) leads to a drastic modification in the spatial distribution of the W 4f signal intensity: a larger number of holes inside the flake can be seen, as well as an increase of their size. Moreover, the number of 3D gold features around the flake is significantly increased. In order to better understand the impact of the annealing process on the morphology of the WS_2/Au/mica system, SEM images have been taken ex situ after the SPEM measurements. A large-scale SEM micrograph is shown in Figure 3d: WS_2 flakes of 20–100 μm can be clearly observed as dark contrast features. Moreover, a uniform distribution of bright protrusions can be observed on both the WS_2 flake and the Au/mica substrate. In Figure 3e, a higher magnification of the SEM image is presented: a series of roughly oval structures (marked with red dashed line) scattered throughout the SEM micrograph can be observed, with size ranging from 1 to 8 μm. Their 3D nature is evident in the 3D SEM micrograph rendering shown in Figure 3f. These features are related to blistering or microbubbles, as reported previously [15–18], and they are caused by the clustering of gas trapped between the Au film and the mica substrate during the annealing. Moreover, at higher temperatures (830 K [15]) some of these microbubbles can burst out creating holes in the gold film and exposing mica substrate, as clearly visible in Figure 3e (see black arrows). Comparing the SEM evidence to the SPEM data obtained by in situ annealing in UHV, we can conclude that some microbubbles (marked by white circles) generated at 750 K (Figure 3a) are present underneath the WS_2 flake. When the temperature is raised to 830 K, more and more microbubbles are formed, which eventually burst out producing holes both on the gold and the WS_2 layer (Figure 3c). If we compare the SPEM maps recorded at 750 and 830 K (Figure 3a,c, respectively) it is evident that most microbubbles have exploded at the higher temperature (see white circles in Figure 3a,c, respectively), creating holes in the WS_2 layer. However, the microbubble marked as B1-B3 in Figure 3a–c is still maintained at 830 K.

Since each point in the SPEM image corresponds to a photoemission spectrum within a specific KE range, the variation observed in the relative intensity of the recorded maps in the microbubble regions during the annealing can be associated with a change in the photoemission intensity deriving from the formation of new chemically shifted species. In particular, the contrast change could be connected to a structural transformation produced by the local tensile stress created by the microbubbles on the Au layer, which can be transferred to the WS_2 overlayer because of the strong adhesion energy between the gold and the TMDC layer [19,26]. Therefore, to investigate the nature of the changes induced by strain, μ-PE single spectra of the W 4f and S 2p core-levels (see Figure 4a,b) have been recorded at specific points (defined as A2, B1, B2 and B3 in Figure 3 and reported in Table 1).

Consider the point labelled as A2, which during the annealing at 750 K does not undergo any change in the SPEM contrast compared to same point in the room temperature intensity map (A1 point in Figure 2). On this point, the W 4f and S 2p core-level spectra recorded at 750 K show the typical photoemission spectra of 2H-WS_2 (Figure 4a,b) with a S:W ratio of 2.0:1.0, as in the pristine not annealed film. On the contrary, in the case of the photoemission spectra recorded where a microbubble forms (and eventually bursts out, the B series in Figure 3), the W 4f line shows remarkable changes during the thermal treatments. The W 4f spectrum at 750 K shows three distinct doublets: one intense component with the W $4f_{7/2}$ peak centered at 32.7 eV, which is due to the 2H-WS_2 phase and accounts for 90% of the overall intensity; and a second and third component with the W $4f_{7/2}$ peak maxima at 31.9 eV and 31.3 eV that account for 1.9% and 7.5% of the overall intensity, respectively. Similarly, a new doublet shifted toward lower BE of ~0.8 eV with respect

to 2H phase is also observed for the S 2p peak with the intensity of 2%. The component at 31.3 eV observed in the W 4f spectrum can be related to metallic tungsten, whereas that at 31.9 eV can be associated to the 1T phases, as reported in the literature [25,27,28]. To confirm this attribution, we also evaluated the S/W atomic ratio, taking into account either the main components of the 2H phase or those downshifted by ~0.8 eV, obtaining in both cases a S:W ratio of ~2 (see Table 1).

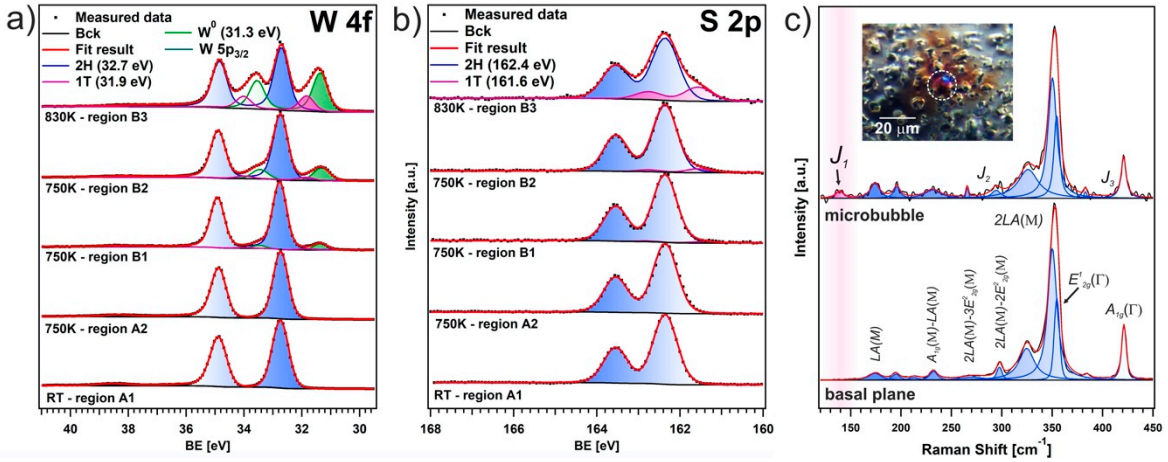

Figure 4. Single energy distribution curves of μ-PE spectra of the W 4f (**a**) and S 2p (**b**) core levels, taken during the in situ annealing process on the regions indicated in Figures 2 and 3. (**c**) Micro-Raman spectra obtained on the basal plane and microbubble region under 532 nm excitation with a spot diameter of about 1.1 μm and an incident power of 100 μW; inset: optical micrograph that shows a microbubble region (white dashed circle).

An independent validation of this hypothesis can be obtained by the analysis of the Raman spectra recorded ex situ after the SPEM experiments (see Figure 4c). Actually, the Raman spatial resolution makes it possible to extract similar information from specific regions as in the case of SPEM experiments. The Raman spectrum recorded on the basal plane of a WS_2 flake is dominated by the first-order modes: LA(M), $E^1{}_{2g}(\Gamma)$ and $A_{1g}(\Gamma)$ and several other second-order peaks that are typically observed for monolayer 2H-WS_2 [29]. On the other hand, on the regions where a microbubble is present, the formation of the 1T-phase is substantiated by the presence of the additional modes J_1 (138 cm^{-1}), J_2 and J_3 that are attributed to the distorted 1T superlattice structure phase [30,31].

Overall, the SPEM maps (Figure 2 vs. Figure 3) indicate a progressive etching of the WS_2 flakes during the thermal treatment. This suggest that in the annealing conditions the layer is not stable. Likely sulfur atoms, especially at the edges or around defects, can react with gaseous species in the background atmosphere, such as O_2, H_2O or H_2 and forming volatile H_2S or SO_x. As a matter of fact, we have also annealed in situ the flakes in presence of a hydrogen background (background hydrogen pressure 1×10^{-5} mbar) and the corresponding SPEM maps (not reported) clearly show an increased etching. The removal of sulfur is confirmed by the atomic ratio between S/W (see Table 1) determined on the basis of the μ-PE spectra, and by the significant formation of a metallic W component in the W 4f core levels. At the end of the thermal treatment, roughly 50% of the 2H-WS_2 been has been converted: a major part formed a metal phase (33%) and a smaller one the 1T phase (13.5%). It has to be noted however that both the WS_2 polymorphs present a large number of anion vacancies already at 750 K (see Table 1).

It is worth noting that the presence of sulfur vacancies in the film plays important role since defect-free MoX_2 monolayers would require a tensile strain of 10–15% to make the 1T phase more energetically favorable. On the other hand, according to a previous theoretical work [32], the presence of vacancies strongly reduces the threshold strain that is necessary to trigger the transition. Moreover, such threshold is further decreased with increasing defect concentration. Our results experimentally corroborate the theoretical predictions

and definitely demonstrate that the synergistic combination of strain induced by the bubble underneath, and of the progressive introduction of vacancies (facilitated by the annealing in H_2), improves the possibility of transforming the 2H phase into the 1T phase.

4. Conclusions

In conclusion, our proof-of-concept experiment demonstrates that phase engineering in TMDCs is possible by manipulation of the strain with spatial resolution. This can be achieved by exploiting flexible substrates, supports with special morphology or by manipulation techniques based on scanning probes. The control of polymorphism paves the way toward the realization of in-plane lateral micrometric heterojunctions between different TMDCs phases, which can be of relevance in advanced electronic devices [9], phase change memory [33,34], ohmic contacts [35,36] and electrocatalysis [37] applications, among others. Our work demonstrates that phase engineering can be obtained on WS_2, whereas in the literature this has also been achieved on tellurides [13,14]. However, theoretical investigations consistently report that many other TMDCs can undergo phase transitions as a function of mechanical strain. This suggests that our results are very general and can be extended to other 2D materials, and other supports with tailorable morphology, representing therefore an enabling technology for the realization of advanced materials and devices.

Author Contributions: Conceptualization, T.K., S.A., G.G., C.M.; methodology, T.K., S.A., L.G., M.A.; investigation, T.K., H.S., P.P.; writing—original draft preparation, T.K.; writing—review and editing, S.A., G.G., L.G., M.A. All authors have read and agreed to the published version of the manuscript.

Funding: This work was partially supported by the following projects: from the Italian MIUR (PRIN 2015: SMARTNESS, 2015K7FZLH; PRIN2017: Multi-e, 20179337R7), and MAECI Italy-China bilateral project (GINSENG, PGR00953). CM would like to acknowledge the award of the University Research Fellowships Renewals 2017 (UF160539) by the Royal Society UK.

Data Availability Statement: The data presented in this study are available free of charge from the corresponding author.

Conflicts of Interest: The authors declare no conflict of interest.

References

1. Manzeli, S.; Ovchinnikov, D.; Pasquier, D.; Yazyev, O.V.; Kis, A. 2D transition metal dichalcogenides. *Nat. Rev. Mater.* **2017**, *2*. [CrossRef]
2. Kosmala, T.; Mosconi, D.; Giallongo, G.; Rizzi, G.A.; Granozzi, G. Highly Efficient MoS2/Ag2S/Ag Photoelectrocatalyst Obtained from a Recycled DVD Surface. *ACS Sustain. Chem. Eng.* **2018**, *6*, 7818–7825. [CrossRef]
3. Kosmala, T.; Coy Diaz, H.; Komsa, H.-P.; Ma, Y.; Krasheninnikov, A.V.; Batzill, M.; Agnoli, S. Metallic Twin Boundaries Boost the Hydrogen Evolution Reaction on the Basal Plane of Molybdenum Selenotellurides. *Adv. Energy Mater.* **2018**, *8*, 1800031. [CrossRef]
4. Wang, Q.H.; Kalantar-Zadeh, K.; Kis, A.; Coleman, J.N.; Strano, M.S. Electronics and optoelectronics of two-dimensional transition metal dichalcogenides. *Nat. Nanotechnol.* **2012**, *7*, 699–712. [CrossRef] [PubMed]
5. Liu, Y.; Duan, X.; Huang, Y.; Duan, X. Two-dimensional transistors beyond graphene and TMDCs. *Chem. Soc. Rev.* **2018**, *47*, 6388–6409. [CrossRef] [PubMed]
6. Li, H.; Shi, Y.; Chiu, M.H.; Li, L.J. Emerging energy applications of two-dimensional layered transition metal dichalcogenides. *Nano Energy* **2015**, *18*, 293–305. [CrossRef]
7. Voiry, D.; Yamaguchi, H.; Li, J.; Silva, R.; Alves, D.C.B.; Fujita, T.; Chen, M.; Asefa, T.; Shenoy, V.B.; Eda, G.; et al. Enhanced catalytic activity in strained chemically exfoliated WS2 nanosheets for hydrogen evolution. *Nat. Mater.* **2013**, *12*, 850–855. [CrossRef]
8. Friedman, A.L.; Hanbicki, A.T.; Perkins, F.K.; Jernigan, G.G.; Culbertson, J.C.; Campbell, P.M. Evidence for Chemical Vapor Induced 2H to 1T Phase Transition in MoX2 (X = Se, S) Transition Metal Dichalcogenide Films. *Sci. Rep.* **2017**, *7*, 1–9. [CrossRef]
9. Eda, G.; Fujita, T.; Yamaguchi, H.; Voiry, D.; Chen, M.; Chhowalla, M. Coherent atomic and electronic heterostructures of single-layer MoS 2. *ACS Nano* **2012**, *6*, 7311–7317. [CrossRef]
10. Deng, S.; Sumant, A.V.; Berry, V. Strain engineering in two-dimensional nanomaterials beyond graphene. *Nano Today* **2018**, *22*, 14–35. [CrossRef]
11. Duerloo, K.A.N.; Li, Y.; Reed, E.J. Structural phase transitions in two-dimensional Mo-and W-dichalcogenide monolayers. *Nat. Commun.* **2014**, *5*. [CrossRef] [PubMed]

12. Ghorbani-Asl, M.; Zibouche, N.; Wahiduzzaman, M.; Oliveira, A.F.; Kuc, A.; Heine, T. Electromechanics in MoS2 and WS2: Nanotubes vs. monolayers. *Sci. Rep.* **2013**, *3*, 1–8. [CrossRef] [PubMed]
13. Song, S.; Keum, D.H.; Cho, S.; Perello, D.; Kim, Y.; Lee, Y.H. Room Temperature Semiconductor-Metal Transition of MoTe2 Thin Films Engineered by Strain. *Nano Lett.* **2016**, *16*, 188–193. [CrossRef] [PubMed]
14. Apte, A.; Kochat, V.; Rajak, P.; Krishnamoorthy, A.; Manimunda, P.; Hachtel, J.A.; Idrobo, J.C.; Syed Amanulla, S.A.; Vashishta, P.; Nakano, A.; et al. Structural Phase Transformation in Strained Monolayer MoWSe2 Alloy. *ACS Nano* **2018**, *12*, 3468–3476. [CrossRef]
15. Hummel, R.E.; DeHoff, R.T.; Matts-Goho, S.; Goho, W.M. Thermal grooving, thermotransport and electrotransport in doped and undoped thin gold films. *Thin Solid Films* **1981**, *78*, 1–14. [CrossRef]
16. Kwon, J.Y.; Yoon, T.S.; Kim, K.B.; Min, S.H. Comparison of the agglomeration behavior of Au and Cu films sputter deposited on silicon dioxide. *J. Appl. Phys.* **2003**, *93*, 3270–3278. [CrossRef]
17. Ruffino, F.; Grimaldi, M.G. Template-confined dewetting of Au and Ag nanoscale films on mica substrate. *Appl. Surf. Sci.* **2013**, *270*, 697–706. [CrossRef]
18. Andrew, R.; Krasevec, V. Grain coarsening and gas bubbles in annealed gold films. *Philos. Mag.* **1975**, *31*, 1295–1306. [CrossRef]
19. Desai, S.B.; Madhvapathy, S.R.; Amani, M.; Kiriya, D.; Hettick, M.; Tosun, M.; Zhou, Y.; Dubey, M.; Ager, J.W.; Chrzan, D.; et al. Gold-Mediated Exfoliation of Ultralarge Optoelectronically-Perfect Monolayers. *Adv. Mater.* **2016**, *28*, 4053–4058. [CrossRef]
20. Reale, F.; Palczynski, P.; Amit, I.; Jones, G.F.; Mehew, J.D.; Bacon, A.; Ni, N.; Sherrell, P.C.; Agnoli, S.; Craciun, M.F.; et al. High-Mobility and High-Optical Quality Atomically Thin WS2. *Sci. Rep.* **2017**, *7*, 1–10. [CrossRef]
21. ESCA Microscopy Beamline of Elettra Synchrotron Radiation Facility (Trieste, Italy). Available online: https://www.elettra.trieste.it/elettra-beamlines/escamicroscopy.html (accessed on 20 November 2020).
22. Bozzini, B.; Amati, M.; Gregoratti, L.; Kiskinova, M. In-situ Photoelectron Microspectroscopy and Imaging of Electrochemical Processes at the Electrodes of a Self-driven Cell. *Sci. Rep.* **2013**, *3*, 1–5. [CrossRef] [PubMed]
23. Cattelan, M.; Markman, B.; Lucchini, G.; Das, P.K.; Vobornik, I.; Robinson, J.A.; Agnoli, S.; Granozzi, G. New Strategy for the Growth of Complex Heterostructures Based on Different 2D Materials. *Chem. Mater.* **2015**, *27*, 4105–4113. [CrossRef]
24. Martinez, H.; Benayad, A.; Gonbeau, D.; Vinatier, P.; Pecquenard, B.; Levasseur, A. Influence of the cation nature of high sulfur content oxysulfide thin films MO y S z (M = W, Ti) studied by XPS. *Appl. Surf. Sci.* **2004**, *236*, 377–386. [CrossRef]
25. Lin, Y.C.; Yeh, C.H.; Lin, H.C.; Siao, M.D.; Liu, Z.; Nakajima, H.; Okazaki, T.; Chou, M.Y.; Suenaga, K.; Chiu, P.W. Stable 1T Tungsten Disulfide Monolayer and Its Junctions: Growth and Atomic Structures. *ACS Nano* **2018**, *12*, 12080–12088. [CrossRef] [PubMed]
26. Torres, J.; Zhu, Y.; Liu, P.; Lim, S.C.; Yun, M. Adhesion Energies of 2D Graphene and MoS2 to Silicon and Metal Substrates. *Phys. Status Solidi (A) Appl. Mater. Sci.* **2018**, *215*, 1–8. [CrossRef]
27. Mahler, B.; Hoepfner, V.; Liao, K.; Ozin, G.A. Colloidal synthesis of 1T-WS2 and 2H-WS2 nanosheets: Applications for photocatalytic hydrogen evolution. *J. Am. Chem. Soc.* **2014**, *136*, 14121–14127. [CrossRef]
28. Lunardon, M.; Ran, J.; Mosconi, D.; Marega, C.; Wang, Z.; Xia, H.; Agnoli, S.; Granozzi, G. Hybrid Transition Metal Dichalcogenide/Graphene Microspheres for Hydrogen Evolution Reaction. *Nanomaterials* **2020**, *10*, 2376. [CrossRef]
29. Berkdemir, A.; Gutiérrez, H.R.; Botello-Méndez, A.R.; Perea-López, N.; Elías, A.L.; Chia, C.I.; Wang, B.; Crespi, V.H.; López-Urías, F.; Charlier, J.C.; et al. Identification of individual and few layers of WS2 using Raman Spectroscopy. *Sci. Rep.* **2013**, *3*, 1–8. [CrossRef]
30. Loh, T.A.J.; Chua, D.H.C.; Wee, A.T.S. One-step Synthesis of Few-layer WS2 by Pulsed Laser Deposition. *Sci. Rep.* **2015**, *5*, 1–9. [CrossRef]
31. Pierucci, D.; Zribi, J.; Livache, C.; Gréboval, C.; Silly, M.G.; Chaste, J.; Patriarche, G.; Montarnal, D.; Lhuillier, E.; Ouerghi, A.; et al. Evidence for a narrow band gap phase in 1T′ WS2 nanosheet. *Appl. Phys. Lett.* **2019**, *115*, 032102. [CrossRef]
32. Tang, Q. Tuning the phase stability of Mo-based TMD monolayers through coupled vacancy defects and lattice strain. *J. Mater. Chem. C* **2018**, *6*, 9561–9568. [CrossRef]
33. Duerloo, K.A.N.; Reed, E.J. Structural phase transitions by design in monolayer alloys. *ACS Nano* **2016**, *10*, 289–297. [CrossRef] [PubMed]
34. Li, Y.; Duerloo, K.A.N.; Wauson, K.; Reed, E.J. Structural semiconductor-to-semimetal phase transition in two-dimensional materials induced by electrostatic gating. *Nat. Commun.* **2016**, *7*, 1–8. [CrossRef] [PubMed]
35. Kappera, R.; Voiry, D.; Yalcin, S.E.; Branch, B.; Gupta, G.; Mohite, A.D.; Chhowalla, M. Phase-engineered low-resistance contacts for ultrathin MoS2 transistors. *Nat. Mater.* **2014**, *13*, 1128–1134. [CrossRef] [PubMed]
36. Cho, S.; Kim, S.; Kim, J.H.; Zhao, J.; Seok, J.; Keum, D.H.; Baik, J.; Choe, D.; Chang, K.J.; Suenaga, K.; et al. Phase patterning for ohmic homojunction contact in MoTe2. *Science* **2015**, *349*, 625–628. [CrossRef] [PubMed]
37. Wang, J.; Huang, Y.; Ma, F.; Zhang, J.; Wei, X.; Liu, J. Strain engineering the electronic and photocatalytic properties of WS 2 /blue phosphene van der Waals heterostructures. *Catal. Sci. Technol.* **2020**. [CrossRef]